MODELLING OF STATIC AERODYNAMICS OF HELICOPTER UNDERSLUNG LOADS

D I Greenwell
Centre for Aeronautics, City University, London

Keywords: *underslung loads, bluff bodies, aerodynamic modelling, MILVAN, CONEX*

Abstract

The complex aerodynamics of rectangular underslung helicopter loads can lead to severe stability problems, but are difficult to represent in flight dynamics models. Current models for box aerodynamics are highly unsatisfactory, being entirely empirical and requiring large amounts of experimental data to generate. This paper presents a new modelling approach, which takes account of the bluff-body nature of the flow, where loads are dominated by normal pressure forces. Existing experimental data is recast in body-axes form, with α and β replaced by velocity components perpendicular and parallel to the box faces. Force and moment data for a wide range of boxes then collapse onto a set of simple generic characteristics, with features that can be related directly to the underlying flow physics. Modelling of container aerodynamics is greatly simplified, and allowance for effects of turbulence, Reynolds Number, wind tunnel interference and geometry modifications becomes possible.

1 Introduction

An important but hazardous aspect of military & civil helicopter operations is the carrying of underslung loads. For many loads, the maximum speed at which they may be carried is limited not by the available power, but by the (often sudden) onset of instabilities. Three basic types of instability [1] can occur:

1. Aerodynamic instability of the load
2. Helicopter and load vertical oscillations
3. Sling cable flapping

which can force the helicopter pilot to reduce speed quickly, or to jettison the load. For aerodynamic instabilities, the initial load motion is typically a periodic yaw oscillation which then couples into the sling and helicopter response, leading to a range of rather complex lateral and longitudinal pendulum modes. Rectangular box loads (for example the 8ft×6ft×6ft CONEX or 8ft×8ft×20ft MILVAN cargo containers) are particularly susceptible to aerodynamic instabilities, especially when lightly loaded [2].

Considerable effort has been put into the simulation of underslung load instabilities, with various authors developing increasingly sophisticated models of the system dynamics. Stuckey [3] gives a useful review of the field up till 2001; current research groups working in this field include NASA Ames (with Northern Arizona University) [4], Delft University [5] and Liverpool University [6].

For the specific case of aerodynamic instabilities, it is clearly important to model both the static and dynamic aerodynamic characteristics of the load. However, constructing adequate aerodynamic models of rectangular box loads for simulation purposes has proven rather difficult, since the large-scale separated flows typical of these bluff bodies lead to highly non-linear and time-dependent aerodynamic characteristics. As a consequence, models rely heavily on experimental data (although some limited progress is being made now on CFD predictions of load aerodynamics [7]).

Unfortunately, obtaining good quality experimental data is also difficult, since:

- achieving the necessary wide range of angle of attack (> ±40°) and sideslip (±180°) in a conventional wind tunnel is often not possible, leading to a need for extrapolation from a limited α,β incidence domain [8],
- robust model support systems are needed, leading to very high levels of interference, which cannot be accounted for using conventional 'attached flow' tares [8],
- Reynolds Number and turbulence effects on bluff-body aerodynamics are still poorly understood, particularly for 3D flows [9],
- dynamic testing of bluff bodies requires specialized rigs and data analysis techniques [10], and
- the combination of separated flow and large-amplitude motion means that, unlike conventional aircraft, there is no simple theoretical analysis for the characteristics of a rectangular box upon which to build an aerodynamic model.

Current 'static' aerodynamic models are therefore largely based on empirical representations of wind-tunnel data from small-scale tests, with extrapolation rules based on geometric symmetry considerations. The sophistication of these models varies widely, covering:

- linearised (small-amplitude) stability derivatives [11],
- derivatives augmented by geometric factors for large pitch/yaw angles [5],
- empirical fits to large-amplitude tunnel data [12],
- comprehensive look-up tables [13].

Dynamic wind tunnel test data for 3D box loads is very limited, and rather inconsistent, so many models do not include any dynamic effects at all. Those that do again use a range of techniques, with varying degrees of success:

- simple damping terms [12],
- conventional dynamic derivatives [14],
- transfer function fits to frequency-dependent derivatives [15], [16].

The current situation for modelling rectangular box static and dynamic aerodynamics is highly unsatisfactory. Models used are essentially empirical, requiring large amounts of wind tunnel (or CFD) data to generate, and providing no rational basis for correction of Reynolds Number, free-stream turbulence, and support interference effects. These models give no insight into the underlying flow physics, and do not provide any means for prediction of the aerodynamic characteristics of new (or modified) load geometries.

As a first step to addressing these problems, this paper presents an alternative approach to static modelling of rectangular loads, based on the use of

a) a more appropriate form for the basic aerodynamic model structure, and
b) the partition of the characteristics into elements related to readily identifiable features of the basic bluff-body flow.

By establishing a physical foundation for a static aerodynamic model, data scaling, correction and extrapolation can be put on a more rigorous footing. In turn, this approach then provides an improved starting point for the inclusion of unsteady dynamic effects.

The model development will proceed in incremental stages:

- a review of the basic features of separated flows on 2D rectangular prisms
- identification of relationships between the flow topology and aerodynamic loads as incidence is varied
- a comparison of 2D and 3D rectangular box aerodynamics for planar (pitch or yaw) motion
- a review of the effect of non-planar motion (combined pitch and yaw)
- a proposal for an alternative set of incidence angles for large-amplitude motion with separated flow, leading on to
- development of a generic six-degree-of-freedom aerodynamic model for rectangular boxes

2 2D Aerodynamics of Rectangular Prisms

2.1 General Features

The basic features of separated flows on 3D rectangular containers are similar to those found on 2D rectangular prisms, which have been the subject of extensive experimental investigation [17] because of their relevance to slender structures (bridges and tall buildings). As sharp-edged bluff bodies, the flows are dominated by separations from the corners. Which corner the flow separates from depends on (a) the incidence angle and (b) the aspect ratio, as shown schematically in Figure 1 [18]. In general, the flow separates from the upstream corners, and for high aspect ratio prisms may then reattach along the sides. As incidence varies, the reattachment points move forward (on the windward side) and aft (on the leeward side).

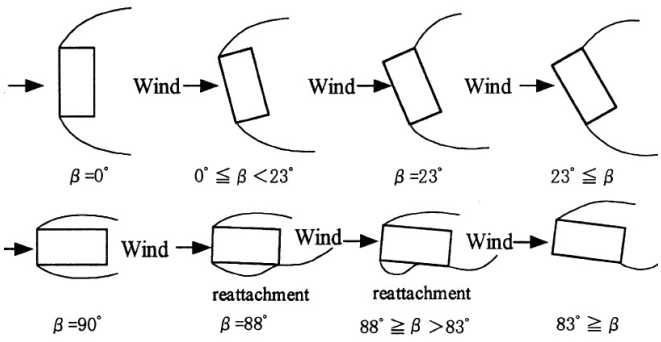

Fig.1 Effect of incidence on 2D separation & reattachment [18]

The basic geometric parameter for a 2D rectangular prism is the aspect ratio, or length/depth ratio L/D. Rather confusingly, many industrial aerodynamics papers call this the height/depth ratio H/D instead. Figure 2 (redrawn from [9] and [17]) shows the variation of drag coefficient (based on frontal area) with length/depth ratio L/D for 2D [17] and 3D [9] shapes.

There is a very distinct change in drag behaviour at a critical ratio of around 0.6, although this is much less marked for 3D boxes. As aspect ratio is increased, the separation topology changes from a flat-plate-like flow at L/D < 0.6 to a more complex flow with separation at the upwind corners, and a small recirculation zone on the side close to the front [19].

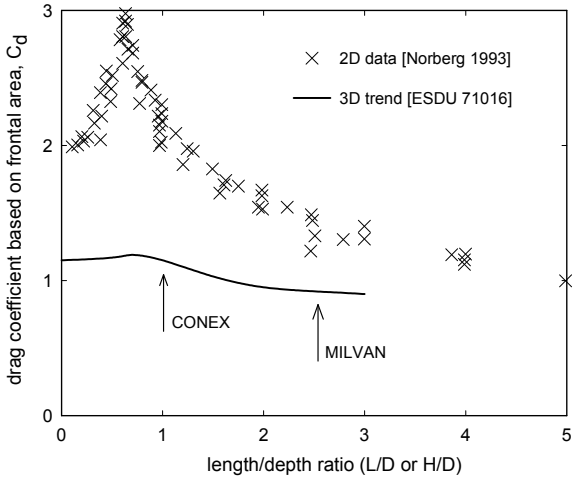

Fig.2 Effect of shape on drag [9][17]

Increasing turbulence (such as that found in the wake of a helicopter rotor) tends to reduce the critical aspect ratio, from 0.6 at normal wind tunnel test conditions to zero for turbulence intensities above around 16% [20]. Typical rectangular box loads lie above the critical aspect ratio (Figure 2), which helps to simplify the modelling task. Another critical point occurs at an L/D of 2.5-3, when the shear layer shed from the front corner re-attaches to the side to form a closed separation bubble. This has no discernible effect on drag, but does correspond to a four-fold increase in the wake Strouhal Number [17] as the wake width suddenly reduces.

The position of the reattachment point has a dominant effect on the aerodynamic characteristics of rectangular prisms at an angle to the flow. For example, Figure 3 shows the variation of lift, drag and pitching moment with pitch angle varying from 0 to 90° for four prisms of aspect ratio 1.0, 1.62, 2.5 and 3 ($B/A \equiv L/D$ [17]). The corresponding aerodynamic characteristics for aspect ratios of 0.62, 0.4 and 0.33 can be obtained by taking 90° as zero incidence. Note that the reference length used in these coefficients is the projected frontal height $D_f = D\cos\alpha + L\sin\alpha$, which varies with pitch angle. The moment reference centre is the centroid of the prism. For each shape, the pitch

angle for which the side face attachment point is at the rear corner is denoted by α_R. Figure 3 clearly shows that this incidence corresponds directly to a break in all three coefficients – lift, drag and pitching moment.

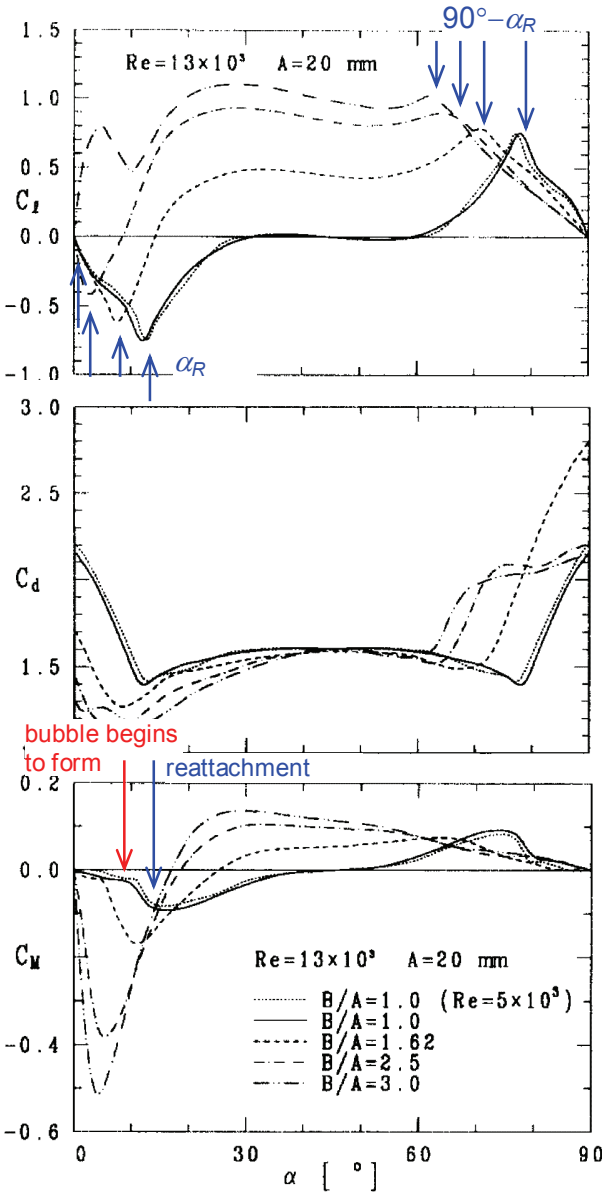

Fig.3 Effect of bubble formation on 2D lift, drag and moment [17] (wind-axis coefficients based on projected frontal area)

From an aeronautical point of view, the effect of pitch angle is rather counter-intuitive. The lift-curve slope for all aspect ratios below 3 is negative for low incidences, which in slender structures can lead to a dynamic instability known as 'galloping'. The drag initially reduces with increasing incidence (although a part of this behaviour in Figure 3 is due to the change in projected frontal area). All aspect ratios are statically stable in pitch at low incidences, and unstable at 45° (although the difference between shapes is again exaggerated by the use of projected height).

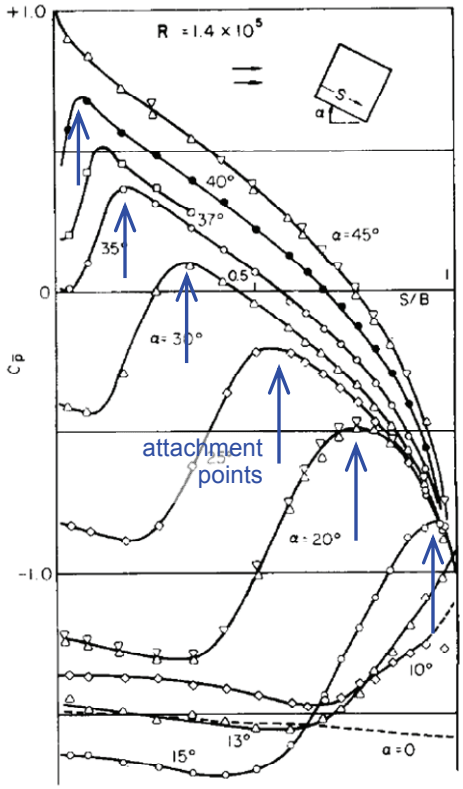

Fig.4 Effect of incidence on pressure distribution under a side face separation bubble [21]

The reasons for this behaviour become apparent when the corresponding side face pressures are examined. For example, Figure 4 shows the pressure distribution on the windward (lower) face of a square prism for pitch angles from 0° to 45° [21]. At zero incidence (face aligned with the freestream) the flow is fully separated, with an almost flat pressure distribution. By 15° the flow has reattached at the trailing edge (see Figure 1) and a classic separation bubble distribution has formed. The overall suction levels remain very high, leading to the negative lift-curve slope seen in Figure 3. The centre of pressure has shifted forward, leading to a negative (stabilising) pitching moment contribution. The base pressure has risen significantly, leading to a drop in drag.

As incidence is increased past 15°, the attachment point moves forward (Figure 1) towards the leading-edge, until at 45° the flow is essentially fully attached. The overall suction levels reduce, contributing to a change in lift from negative to positive. The centre of pressure moves aft, now giving a positive (destabilising) pitching moment contribution. The base pressure remains roughly constant, as does the drag.

The corresponding upper and rear face flows remain fully separated, giving roughly constant pressure distributions. The front face pressures are positive in the region of the stagnation point, which shifts downwards as incidence increases (giving a small negative pitching moment contribution).

2.2 Scaling of 2D Pressure Distributions

Given the significance of the separation bubble contribution to the aerodynamic characteristics of rectangular prisms, it is important to understand how it is affected by geometry and incidence.

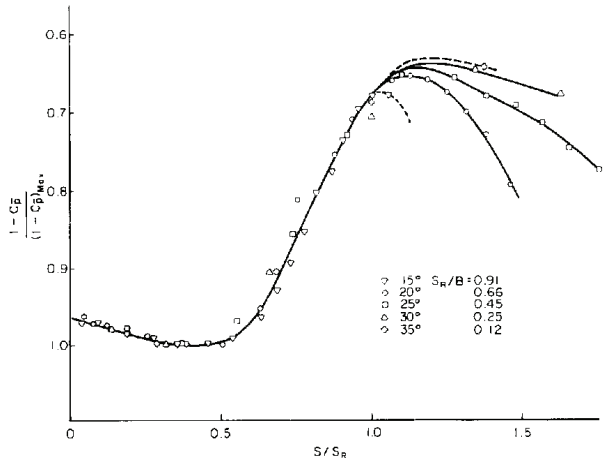

Fig.5 Collapse of separation bubble pressure distribution [21] for a square prism

The pressure distributions in Figure 4 can be split into two elements [21] – a separation bubble of length S (taken from the leading-edge to the attachment point), superimposed on an 'attached flow' which varies from +1 at the leading-edge to the base-pressure at the trailing-edge of the face (Appendix A). Figure 5 from Reference [21] demonstrates that for a square prism the bubble component for a range of incidence (15° to 35°) can be collapsed onto a single distribution by using the bubble length S as a length scale, and the maximum pressure ($1 - C_{pmax}$) at the rear of the bubble as a pressure scale (Figure 5).

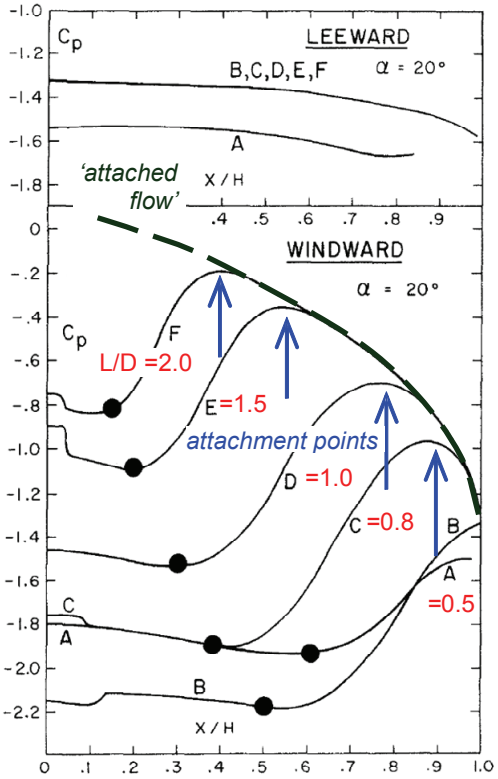

Fig.6 Effect of shape (L/D) on side face pressure distributions at 20° incidence [22]

The same scaling can also be seen in Figure 6 [22] for a range of aspect ratios (L/D = 0.5 to 2.0), at an incidence of 20°. What is also evident from Figure 6 is that the underlying 'attached flow' pressure distribution is the same for each aspect ratio. The same is true of the upper (leeward) surface pressures (except for the sub-critical prism 'A', with $L/D < 0.6$).

Finally, Figure 7 shows that the variation of attachment point location S with incidence for a range of 2D prisms [17][18][21][22][23] can be collapsed onto a single curve, if the frontal height D is used as a length scale. S/D varies from ~3 at 0° to 0 (fully attached) at 45°. The single 3D dataset available (for a 1:1:2.5 MILVAN container model [10]) shows a similar variation, but with the attachment point much further forward at zero incidence.

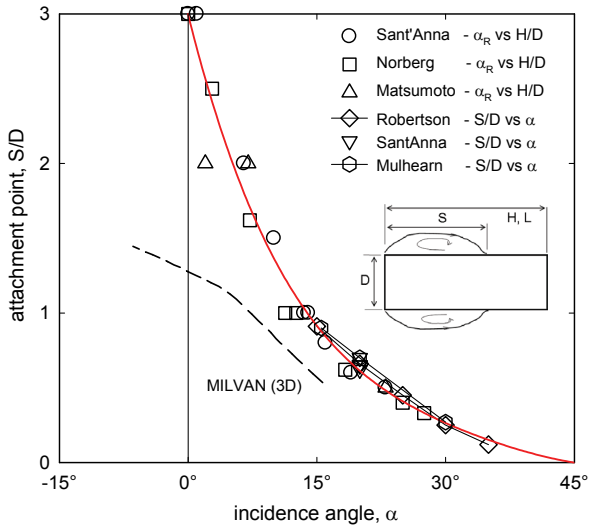

Fig.7 Universal scaling of 2D attachment point

To summarise:

- the side face pressure distribution can be split into a separation bubble superimposed on an 'attached' flow
- the attached flow component varies gradually with incidence (Figures 4 and A1), but is independent of aspect ratio (Figure 6)
- the non-dimensional attachment point *S/D* is a function of incidence only (Figure 7)
- the magnitude of the separation bubble component is a function only of the 'attached' pressure at the attachment point (Figure 5).

2.3 Effect on Forces & Moments

The surface pressures on one face of a rectangular can be integrated to give the mean pressure coefficient (= normal force coefficient based on face area) and moment coefficient (about the mid-face, based on face length *L*) as a function of incidence. Figure 8 shows such an integration for a square prism (based on data in [21] and [9]).

The incidence angle convention here is that of ESDU 71016 [9], and is different from earlier figures, with 0° and 180° corresponding to an orientation perpendicular to the flow, at the front of the prism and rear of the prism respectively. 90° now corresponds to a face oriented parallel to the flow, at the *upper* side of the prism. The pressure curve is symmetric about 0°, and the moment curve is antisymmetric.

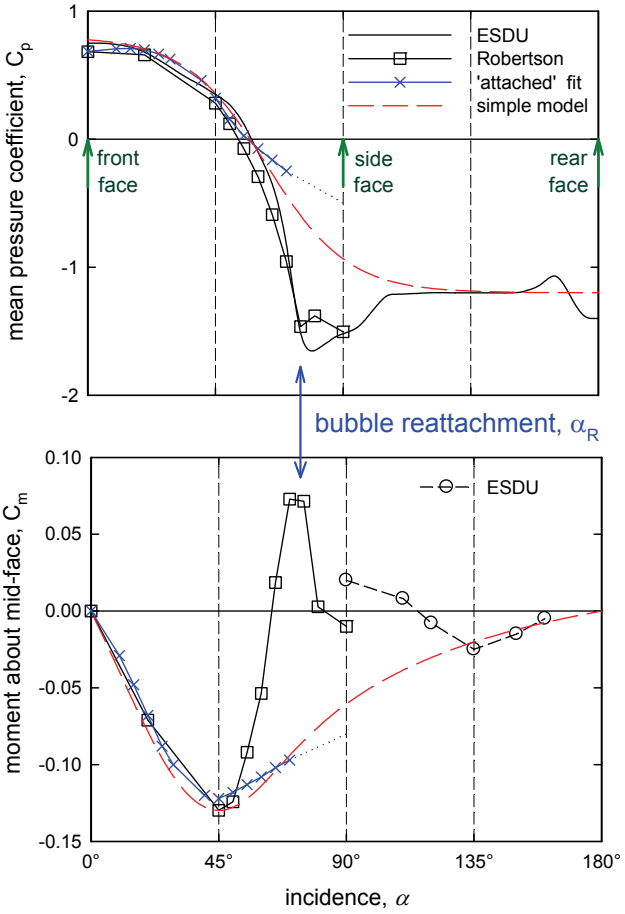

Fig.8 Effect of inclination on mean pressure and moment about mid-face for a square 2D prism [9][21]

Starting at 0°, the face is perpendicular to the oncoming flow, with the stagnation point in the centre giving zero moment and a mean pressure coefficient of the order of +0.7. As pitch angle is increased the face moves upwards and away from the flow. The mean pressure begins to reduce, and the stagnation point moves downwards (Figure A1), giving a negative (stabilising) moment contribution. At 45° the stagnation point has moved to the front corner, with the pressure on the face varying almost linearly from +1 at the leading-edge to the base-pressure at the trailing-edge (Figure 4). The mean pressure is close to zero, while the moment has reached its maximum negative value.

As incidence is increased from 45°, the flow separates at the front corner, and a separation bubble forms. The mean pressure continues to decrease smoothly. The localised high suction under the separation bubble at the leading-edge of the face (Figure 4) gives a positive (destabilising) moment contribution, and the moment curve abruptly reverses. As pitch angle increases the separation bubble grows longer and longer, giving an increasingly negative mean pressure and a moment coefficient changing sign from negative to positive.

Eventually the attachment point reaches the rear of the face (in this case for $S/L = 1$ at about 90°–15° = 75° from Figure 7), and the bubble breaks down into a fully separated flow by 90°. The pitching moment drops to near zero, while the mean pressure begins to rise slightly. From 90° to 180° the mean (base) pressure remains almost constant, at a value which depends on the aspect ratio L/D (Figure 2). The moment coefficient becomes slightly negative, and then comes back to zero at 180°.

From the discussion in Section 2.2, rectangular prisms of higher aspect ratios should behave in a similar manner to Figure 8, with two exceptions. The base pressure at 180° is (less negative), giving lower overall drag (Figure 2), and the reattachment incidence α_R is delayed (eg to 90° for a 3:1 aspect ratio, Figure 7).

2.4 Simplified Modelling

The variation in normal force and moment contribution for a single face discussed above can be used to build up a generic model of the corresponding lift, drag and pitching moment for a complete rectangular prism.

The pressure and moment coefficients in Figure 8 can be represented by a modified exponential fit to the underlying 'attached flow' contribution (red dashed line), extended to cover the full incidence range. The superimposed 'separated flow' contribution can then be represented by a piecewise linear fit between 45° and 135°, with the location of the maximum value given by the reattachment incidence from Figure 7.

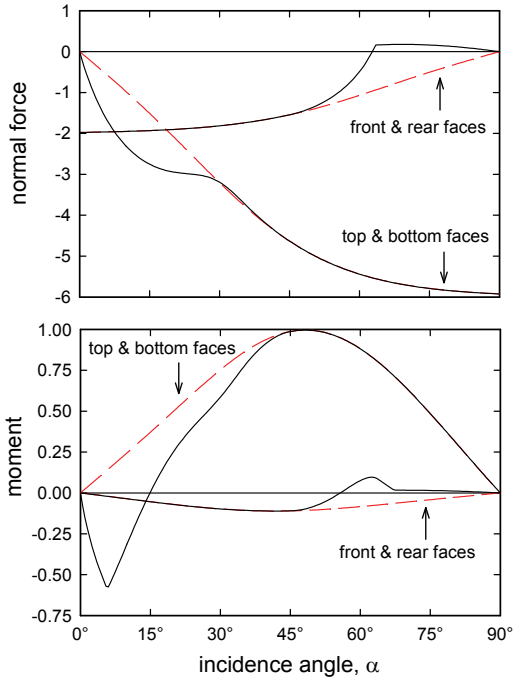

Fig.9 Modelled contribution from opposing faces to force and moment on a 3:1 prism (coefficients based on height D)

Combining the contributions from opposing faces then gives the normal force coefficient (upper and lower faces) and axial force coefficient (front and rear faces). For example, Figure 9 shows these components for a 3:1 prism (with coefficients based on the depth D).

Figure 10 shows the same model results for a range of aspect ratios, but with the axial force and normal force combined into conventional lift and drag coefficients. The projected frontal depth D_f has been used as the reference length, in order to permit a direct comparison with the experimental data of Figure 3. The 'attached flow' contribution to the 3:1 prism is indicated by the red dashed line. A comparison of Figure 3 and Figure 10 clearly demonstrate that this approach captures the basic behaviour of 2D rectangular prisms.

It is also clear that this is not a useful way of presenting the aerodynamic coefficients of a bluff body. The variation in reference length D_f with incidence obscures the basic aerodynamic behaviour, while conventional wind-axis lift and drag coefficients are not appropriate for a rectangular bluff body. In this case, with large-

scale separated flow, the normal pressure loads on each face are much larger than the tangential forces, and so body-axis axial and normal force coefficients would correspond more closely to the underlying flow physics.

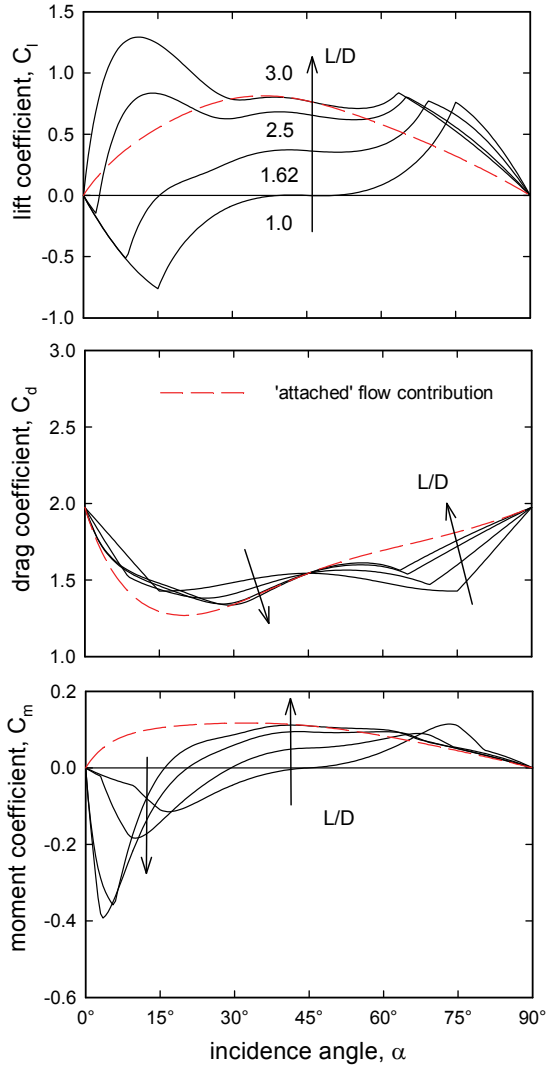

Fig.10 Modelled effect of L/D on 2D prism lift, drag and moment (coefficients as Fig. 3)

The effectiveness of this approach is shown in Figure 11a, which redraws data from Figure 3 [17] as body-axis coefficients based on the corresponding side lengths (denoted by a subscript*). The usual aeronautical sign conventions are applied.

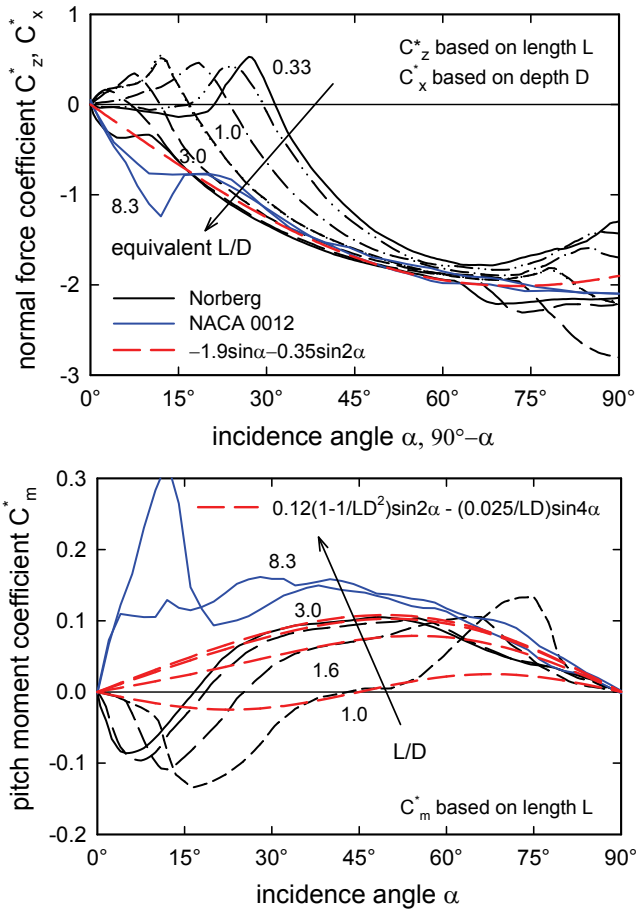

Fig.11 Effect of L/D on body axis force and moment for 2D prisms (coefficients based on the corresponding side length)

The normal force coefficients C_Z^* are based on the upper and lower side length L (with equivalent L/D = 1, 1.62, 2.5 and 3) and plotted vs incidence α. The axial force coefficients C_X^* are based on the front and rear side depth D (with equivalent L/D = 0.33, 0.4, 0.62 and 1), and plotted vs 90°−α for direct comparison with the normal force. Also shown for comparison is the normal force coefficient for a NACA 0012 aerofoil [24] for normal (leading-edge forward) and reversed (trailing-edge forward) orientations.

The normal force coefficients converge to a limiting sine curve (similar to that seen in Figure 9) of

$$C_Z^* \approx -1.9\sin\alpha - 0.35\sin 2\alpha \qquad (1)$$

At low incidences the increased suction due to the separation bubble on the lower surface gives a positive (downward) normal force increment,

with a peak corresponding closely to the attachment angle α_R in Figure 7. (The exception is the relatively narrow NACA 0012 aerofoil, where the upper surface suction dominates and the increment is negative). For aspect ratios greater than critical, the separated flow increment falls to zero at around 45-60°. At very high incidences the base pressure depends on the wake flow structure, which in turn depends in a rather unpredictable way on the aspect ratio L/D.

The pitching moment characteristics are a little more complex, since these combine contributions from both the upper/lower surface and front/rear face pairs. Figure 9 indicates that the basic 'attached flow' contribution from one pair of faces follows a $sin2\alpha$-like curve (with possibly a small skew to the right). From purely geometric considerations, assuming similar aerodynamic behaviour on each face, the moment contribution from the short side will be of opposite sign to that from the long side, and smaller by a factor of $1/(L/D)^2$.

The combined 'attached flow' moment contributions (Figure 11b) can then be represented by an equation of the form

$$C_m^* \approx 0.12\left(1-\left(\frac{D}{L}\right)^2\right)\sin 2\alpha - 0.025\left(\frac{D}{L}\right)\sin 4\alpha \quad (2)$$

where the moment reference length is the length L. The $sin2\alpha$ term is the sum of the opposing moment contributions from the front/rear and upper/lower faces. The additional $sin4\alpha$ term corresponds to the small asymmetry seen in Figure 9, and from the empirical variation with aspect ratio would appear to be dominated by the contribution from the front/rear faces.

For a square prism, the 'attached flow' component (red dashed line in Figure 11b) can be seen to be stabilising at 0° and 90° incidence, and destabilising at 45°. For the other prisms, this component is destabilising at low incidence (short side facing into the flow), but stabilising at high incidence (long side facing into the flow). The 'separated flow' contribution is always stabilising, with a peak increment corresponding closely again to the attachment angle α_R in Figure 7.

3 3D Aerodynamics of Rectangular Containers

In contrast to the 2D case, there is relatively little experimental data available for 3D rectangular loads. There is also a significant level of variation between datasets, due perhaps to the highly unsteady nature of the flow and to the high levels of support interference found with conventional strut mounting.

The majority of published data relates to the 8ft×8ft×20ft MILVAN container ([10][14][25][26][27][28], with a review in [8]), although some more work has been done recently on the 6ft×6ft×8ft CONEX container [29][30]. Only two sources provide any information on effect of shape, Reference [28] from NASA (a data report which forms the basis of almost every MILVAN simulation model), and a rather little-known linked set of reports from RMCS Shrivenham [31][32][33].

3.1 'Planar' Motion (pure α or β)

The basic planar (pure pitch or yaw) aerodynamic characteristics of 3D rectangular boxes are very similar to those of 2D prisms.

For example, Figure 12 shows wind tunnel test data from NASA [28] for three standard boxes – an 8ft cube, an 8ft×8ft×20ft MILVAN container, and an 8ft×8ft×40ft shipping container. The data shown here is for smooth-sided, sharp-edged models, and since the boxes have a square front face, the pitch and yaw aerodynamics are essentially identical. (NB [28] also presents data for models with more representative corrugated surfaces, which rather surprisingly show very similar behaviour). The data has initially been non-dimensionalised using projected frontal area and height, simply in order to give a direct comparison with the 2D data shown in Figure 3 [17].

The variations in lift, drag and pitching moment with (i) incidence, and (ii) aspect ratio L/D are remarkably similar to the 2D case. However, overall magnitudes have reduced, and the 'separated flow' contributions at low incidences are much less pronounced. Nevertheless, it is clear from a comparison of Figures 2 and 12 that the basic box

aerodynamics in 2D and 3D flows are very similar.

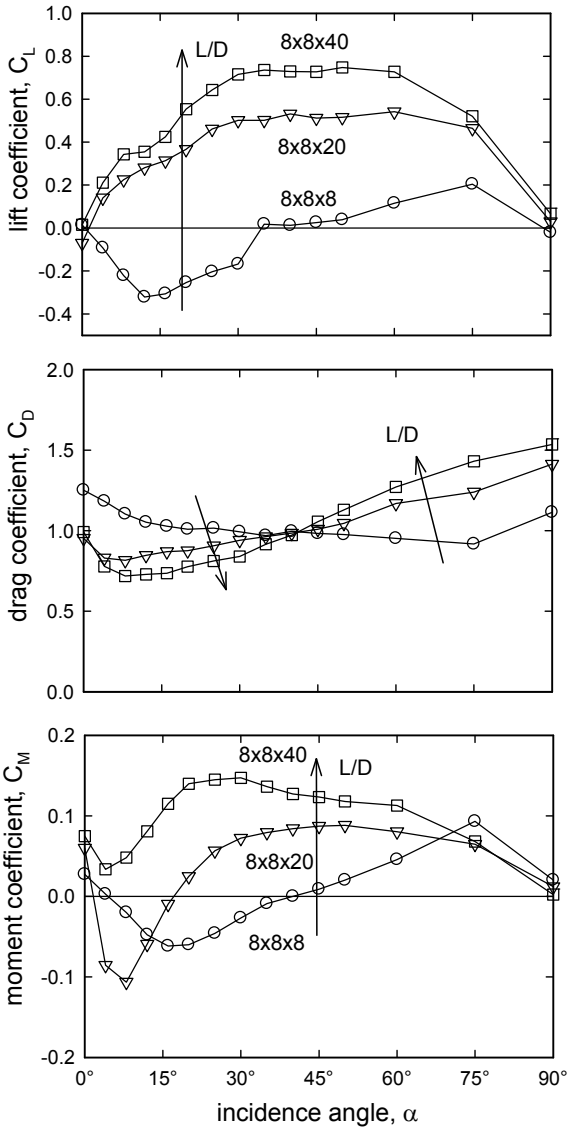

Fig.12 Lift, drag and pitching moment for three rectangular containers (data from [28], coefficients as Fig. 3)

Looking specifically at the MILVAN container, Figure 13 compares published data for wind-axis drag, sideforce and yawing moment variation with yaw angle [8][25][26][27], for models with representative geometry (ie surface corrugations, base skids etc). Since underslung loads oscillate primarily in yaw, available datasets focus on providing a wide (±180°) yaw/sideslip angle range, with often a rather limited (±20-40°) pitch/angle of attack range. MILVAN data is invariably given in wind axes, and usually in terms of forces and moments divided by dynamic pressure (giving units of m^2 and m^3 respectively).

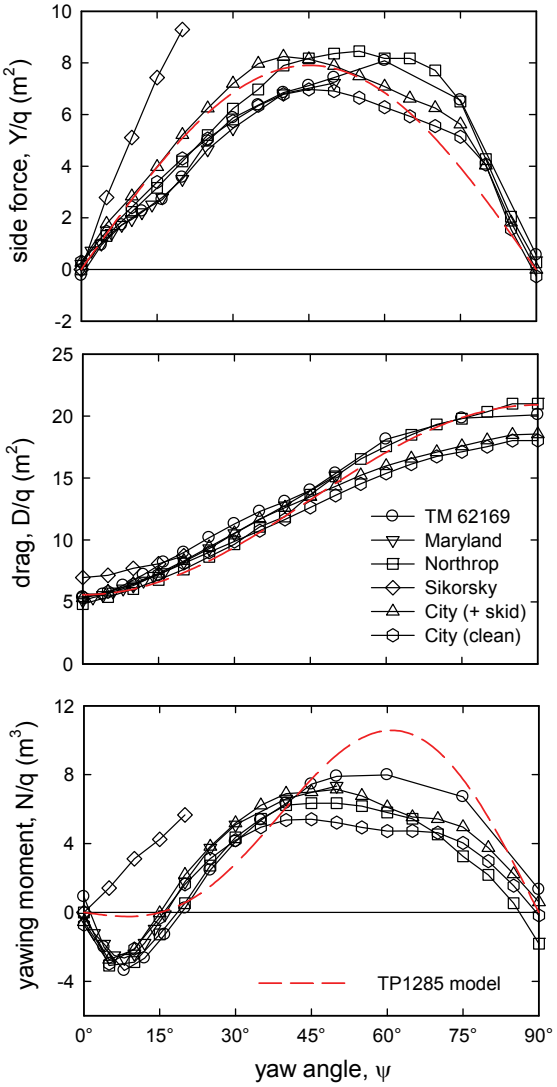

Fig.13 Comparison of MILVAN (8ft×8ft×20ft) aero datasets for planar yawing motion [8][25][26][27]

Two datasets show some variation from the general trend, indicating the significance of support interference in bluff body testing. Early Sikorsky data [26] shows a much higher sideforce at lower incidences, and an unstable yawing moment characteristic. Unpublished data from City University shows a 13% reduction in drag (and a smaller reduction in yawing moment) at higher incidences. The Sikorsky data is typical of excessive interference from too short a support strut (a similar result is reported in [10]), while the tests at City used a multiple-point mounting more

representative of a typical load sling. Reference [8] also notes that support tares for a strut mounted MILVAN model [28] often appeared to be random.

3.2 Non-planar Motion (coupled α and β)

3.2.1 Conventional Representation

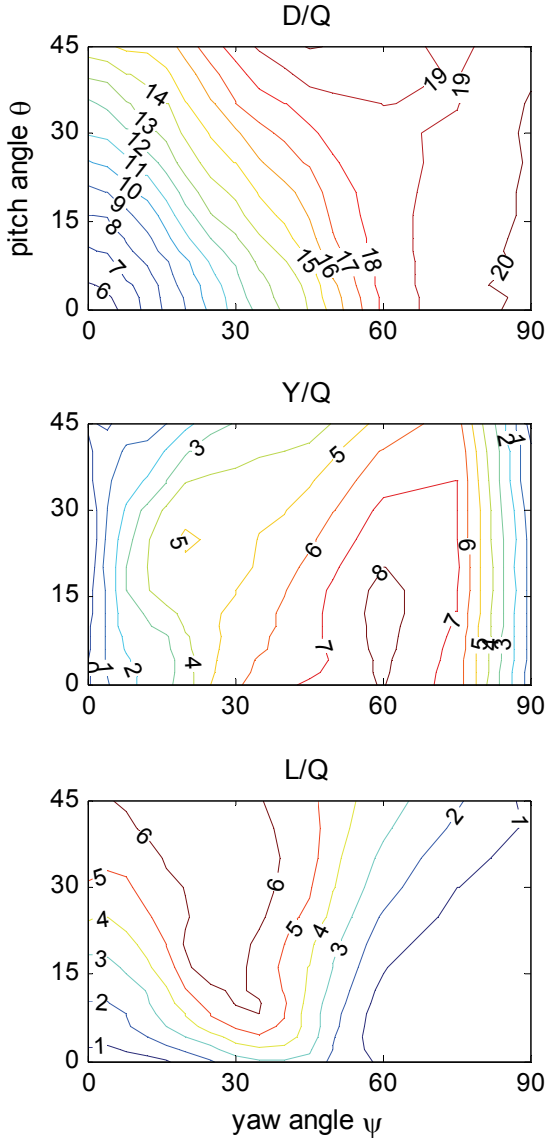

Fig.14a MILVAN drag, sideforce and lift for non-planar (pitch + yaw) motion (wind axes, data from [8])

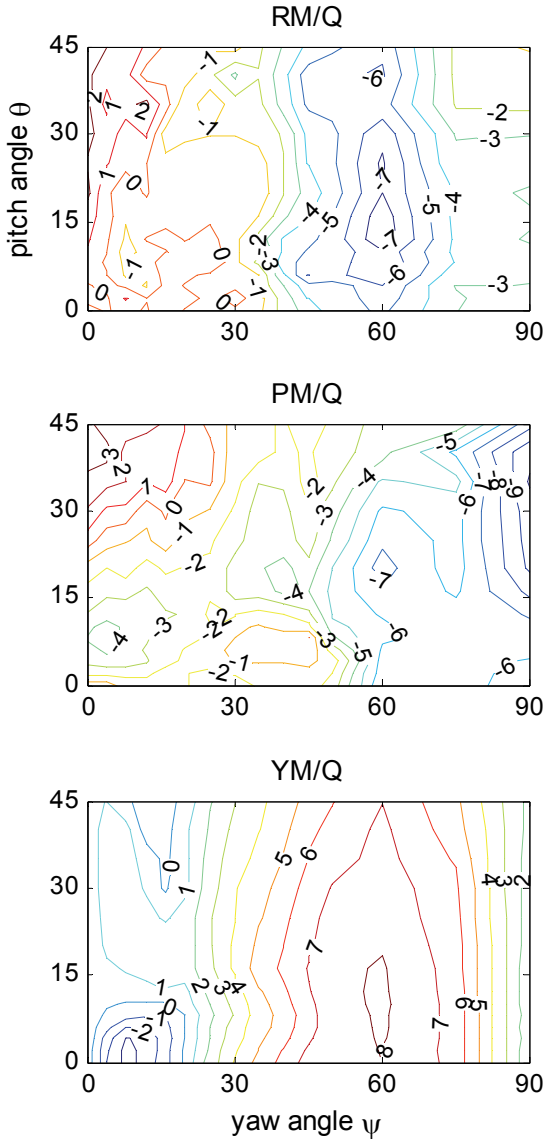

Fig.14b MILVAN rolling, pitching and yawing moments for non-planar (pitch + yaw) motion (wind axes, data from [8])

Having measured these aerodynamic characteristics, the next question is how to represent them within a flight dynamics model. One possibility is to use a large look-up table, but until recently many studies have used curve-

fits to the data. Equation (3) shows a typical example, from a simulation model in [12]. This trigonometric fit to the large-amplitude forces and moments (with an apparent typo in the drag equation), is shown as the red dashed line on Figure 13

$$\begin{aligned} \frac{D}{q} &= 20.9 - 7.66\left(1 + \cos 2\alpha \cos \mathbf{2(?)}\beta\right) \\ \frac{Y}{q} &= -7.9 \sin 2\beta \cos 2\alpha \\ \frac{N}{q} &= -7.73 \sin 2\beta + 4.47 \sin 4\beta \left|\cos \alpha\right| \end{aligned} \tag{3}$$

This type of curve-fit does a reasonable job for sideforce and drag, but clearly struggles with the more complex yawing moment characteristics.

The reasons for this can be seen if a 'full' dataset is examined. Figure 14 shows wind-axis forces (14a) and moments (14b) for a MILVAN model, replotted from tabulated data in [8], which in turn was derived from a careful re-analysis of data from [28]. Note that this data is in dimensional form, ie 'drag area' and 'moment volume'.

The complexity of the data is immediately apparent, and Reference [8] devotes considerable effort to identifying symmetry properties in an attempt to (a) simplify the data representation, and (b) to provide a rational means of correcting for experimental errors and extrapolating to higher pitch angles. The data itself is simply presented as a set of six 2D look-up tables – ie forces and moments as functions of pitch and yaw angle.

3.2.2 Body-Axis Forces

The problem with look-up tables or trigonometric curve-fits to data as complex as that shown in Figure 14, is that neither gives any clue to the underlying flow physics. As a result, any change to container geometry requires the model to be regenerated from scratch – a lengthy and costly process, and hence seldom done.

Such a reliance on empirical modelling should have been a cause for concern before now; but nowhere in the literature has the basic form of the container aerodynamic model ever been questioned.

However, the discussion in Section 2.4 above (and a moment's consideration of the nature of the flow around a box), make it clear that *body-axis* rather than wind-axis forces are the appropriate variables.

Further, what about the aerodynamic parameters, the conventional angle of attack α and sideslip angle β ? These are just one of many possible pairs of incidence angles, and are entirely appropriate for attached flow aerodynamics, but not necessarily for 2D bluff body flows.

Figure 11 gives an indication of a more appropriate definition:

1) the normal force on a given pair of faces is dependent on the angle of the flow relative to those faces,
2) when non-dimensionalised by the corresponding face area, the body-axis coefficients collapse onto a single basic curve, and
3) this basic variation is roughly sinusoidal.

The basic force curves in Figure 11 then become

$$\begin{aligned} C_Z^* &\propto \sin\alpha \propto \frac{w}{V} \\ C_X^* &\propto \sin\left(90° - \alpha\right) \propto \frac{u}{V} \end{aligned} \tag{4}$$

since $\beta = 0$. In other words, the appropriate basic aerodynamic parameters for a rectangular box are the *relative* velocity components perpendicular to each pair of faces. The corresponding incidence parameter for the sideforce C_Y^* would then be v/V.

For non-planar flow a second incidence parameter is required. In order to complete the (u,v,w) triple, an obvious choice is the direction of the cross-flow velocity component parallel to the face in question (Figure 15), since this will govern which edge the flow separates from. The new incidence parameters are then:

$$C_X^* = fn\left(\frac{u}{V},\ \tan^{-1}\frac{w}{v}\right)$$
$$C_Y^* = fn\left(\frac{v}{V},\ \tan^{-1}\frac{w}{u}\right) \qquad (5)$$
$$C_Z^* = fn\left(\frac{w}{V},\ \tan^{-1}\frac{v}{u}\right)$$

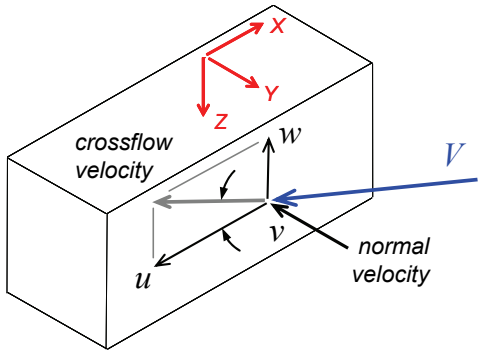

Fig.15 Incidence parameters v/V and tan^{-1}(w/u) for side-face forces and moments

To demonstrate the application of these parameters, Figure 16 shows side-force coefficient C_Y^* for a sharp-edged cube plotted against velocity component normal to the side faces v/V and cross-flow velocity direction relative to the side faces $tan^{-1}(w/u)$, Figure 15.

This data is taken from Reference [30], which is unique in providing not only high quality data over the full (±90°,±180°) pitch/yaw range, but also the results of an extensive study of support interference. Essentially the same results were obtained for C_X^* and C_Z^*.

Symmetry considerations dictate that the 'normal' force is zero at the left-hand edge and constant along the right-hand edge of Figure 16b, and that the plot is symmetric about $tan^{-1}(w/u) = 0$ and antisymmetric about $v/V = 0$.

Immediately, a significant improvement in the data presentation is evident. The overall trend with v/V is almost linear, with very little variation with crossflow direction above $v/V \sim 0.5$. At lower values of v/V there are two symmetrically placed dips in sideforce, centred about cross-flow directions of zero (flow approaching directly from the front of the body) and $\pi/2$ (flow approaching directly from above or below the body). This is the separation bubble contribution discussed previously, which is now much easier to see. At an intermediate cross-flow direction of $\pi/4$ (45°) a closed separation bubble cannot form; instead side-edge vortices on the leeward face maintain essentially an attached flow.

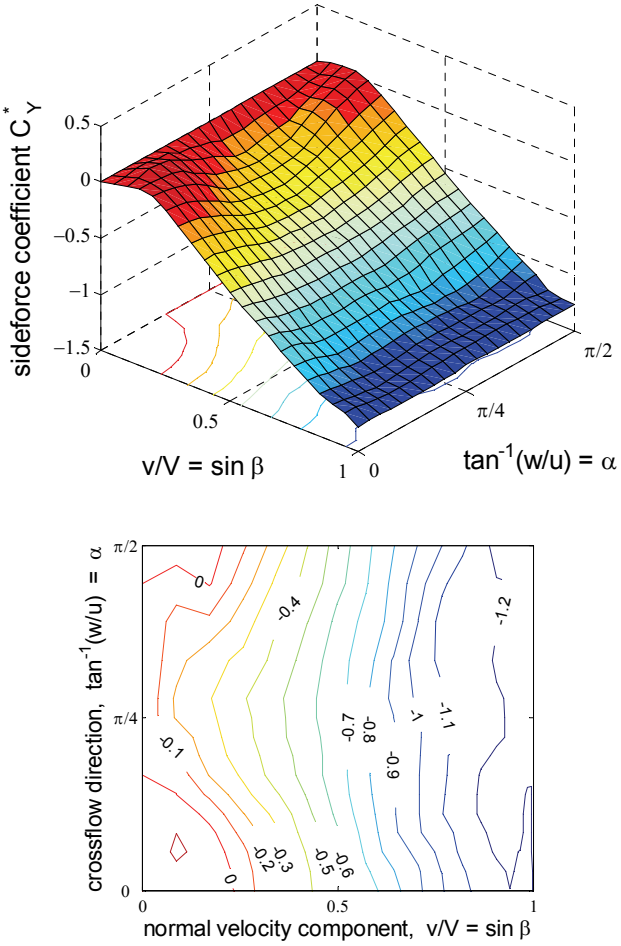

Fig.16 Variation of body axis sideforce coefficient C_Y^* with normal velocity and crossflow direction for a cube (data from [30])

The sharp-edged cube data indicates that this approach has the potential to greatly simplify the modelling of the force data, but as a symmetric object does not provide evidence for its general applicability.

In order to do so, Figure 17 shows the MILVAN model force data from Figure 14 [8] re-plotted using Eqn. (5). The results are very encouraging, with the general form of Figure 16 repeated for all three components, in both shape and magnitude. As one might expect, there is some asymmetry in the 'long' face forces

(sideforce C_Y^* and normal force C_Z^*), due to the 2.5:1 aspect ratio. The dip in the lower left corner in these two plots corresponds to a separation bubble forming from the forward (short) edge, and the dip in the upper left to a larger bubble forming from the side (long) edge.

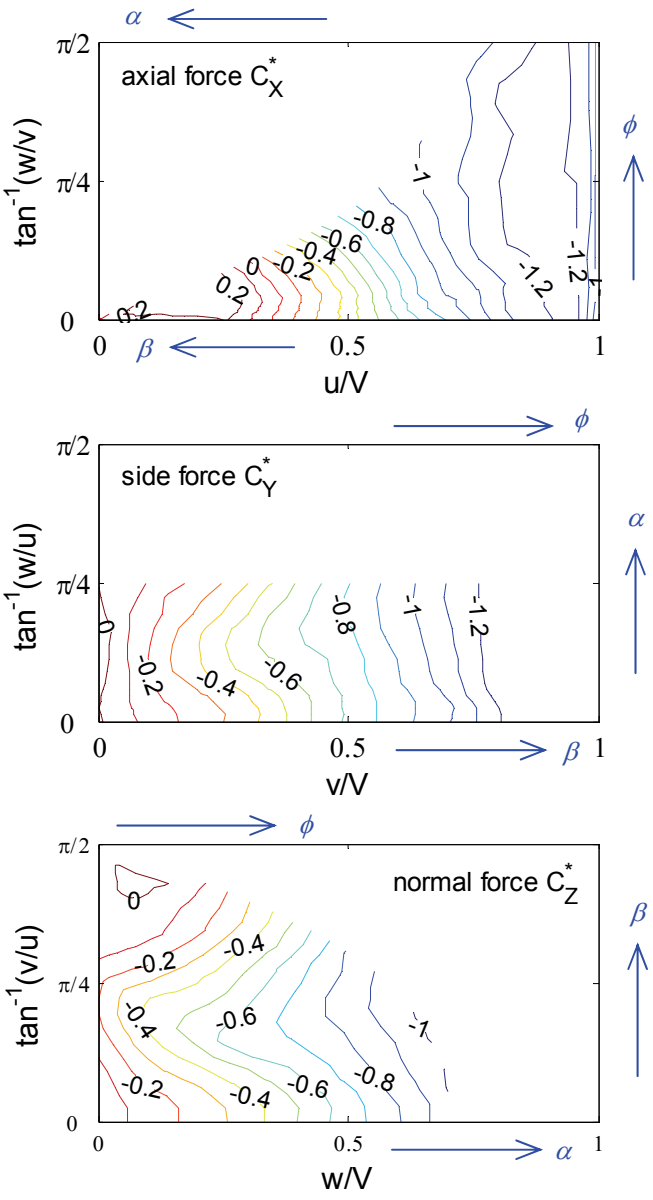

Fig.17 Variation of body axis force coefficients with normal velocity and cross-flow direction for a MILVAN container (data from [8])

Also indicated on Figure 17 for ease of interpretation are the equivalent changes in conventional incidence angles α and β, and roll angle ϕ. For example, on the axial force plot, moving to the left along the lower edge corresponds to increasing sideslip angle, and to the left along the upper edge to increasing angle of attack. Moving upwards along the right-hand edge corresponds to increasing roll angle.

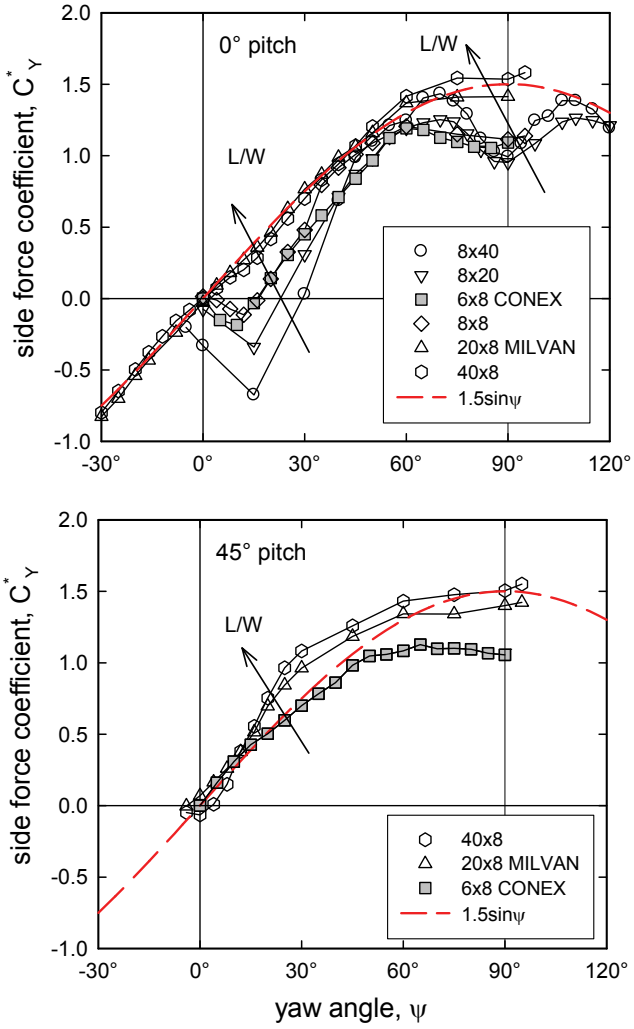

Fig.18 Effect of L/W on 3D body axis force scaling (data from [28][30])

Visual assessments of contour plots are notoriously subjective, so Figure 18 provides a direct comparison of the effect of yaw angle $\psi (= -\beta)$ on sideforce coefficients for a number of strut-mounted box models [28][30], at pitch angles of 0° and 45°. The box geometries are now characterised by their length/width ratio L/W (the appropriate aspect ratio for lateral forces), with $W/D = 1$ in all cases. (NB the 8×40 and 8×20 boxes in Figure 18 are simply the 40×8 and 20×8 boxes from [28] yawed by 90°).

The behaviour at 0° pitch is identical to the 2D prism data in Figure 11a, with all curves converging to a limiting 'attached flow' sine curve

$$C_Y^* \approx 1.5 \sin\psi = -1.5\frac{v}{V} \qquad (6)$$

The 3D lift-curve-slope is reduced from −1.9 to −1.5 compared with 2D flow. As before, the magnitude of the separation bubble contribution reduces, and the peak point moves forward, as aspect ratio L/W increases (and α_R reduces).

The 'base-dip' at high incidences shows a more consistent variation with aspect ratio than for the 2D case, becoming steadily larger as L/W reduces.

At 45° pitch angle the picture is a little less clear. The almost-cubical CONEX container follows the 'attached flow' sine curve, with a large base-dip very similar to the 0° pitch case. The longer boxes (L/W = 2.5 and 5.0) rise above this line before falling back to the same base pressure as at 0° - probably indicating the presence of some vortex lift from a side-edge vortex along the long edge (flow visualisation in [10]).

Further confirmation of the general nature of the normal velocity scaling is given by Figure 19, which re-plots data from [33] for a wide range of higher aspect-ratio box shapes. This dataset from RMCS presents lift and drag variations with pitch angle (up to 40°), for models suspended in the wind-tunnel using a four-point wire mounting. When converted to body-axis form, the majority of the data collapses onto a linear variation with normal velocity component (u/V or w/V), with a slope of −1.2.

The reduction in slope compared with Figure 18 is consistent with the effect of support system seen in Figure 13, indicating that strut mounted model tests may over-predict container drag by 10-20%. As in Figure 18, only boxes with their long side facing the flow (ie $L/W < 1$) show any significant effect of separated flow at lower incidences. This goes from a positive increment for low L/D (lower surface bubble) to negative for high L/D (thin plate with aerofoil-like flow on upper surface). At intermediate incidences some of the slender shapes (high L/D) show signs of a non-linear vortex lift increment similar to that seen on slender wings.

Also of note in Figure 19 is the much later (and smaller) base pressure dip at high incidence, suggesting again that this may be affected by support interference.

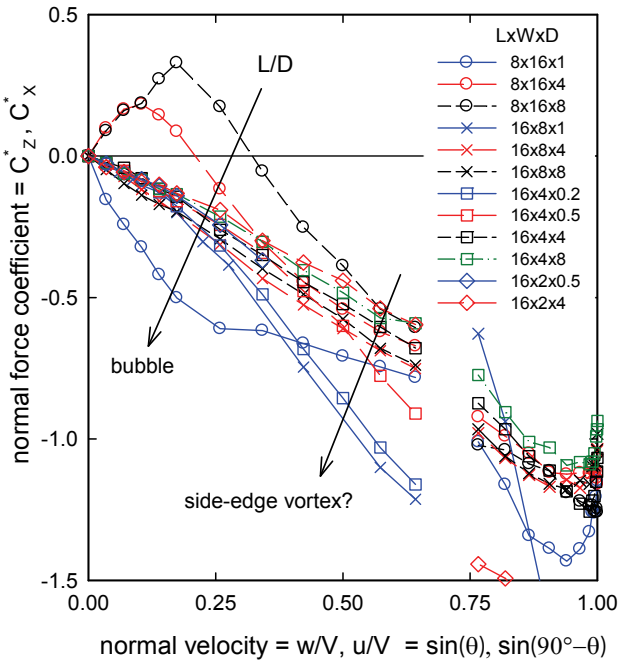

Fig.19 Effect of L/D and W/D on 3D body axis force scaling (data from [33])

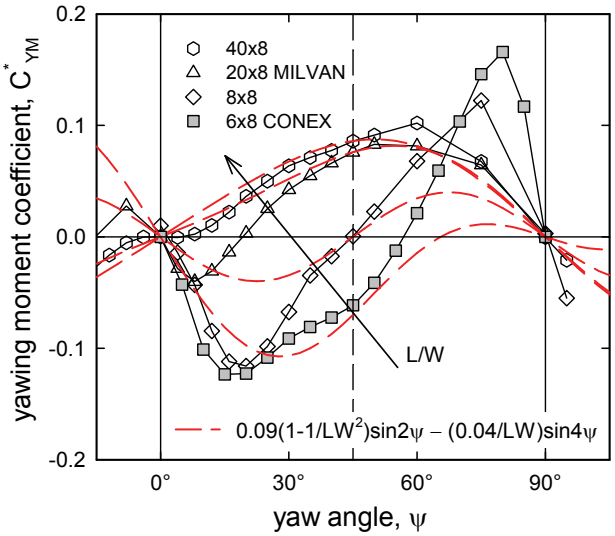

Fig.20 Effect of L/W on 3D moment scaling (yawing moment coefficients based on side face area and length) (data from [28][30])

3.2.3 Body-Axis Moments

The same approach can be applied to body axis moments, with Figure 20 showing that 3D moment characteristics for a range of typical load geometries vary with incidence angle and aspect ratio in a very similar manner to the 2D data in Figure 11b.

The basic 'attached flow' variation (red dashed line) modelled by Eqn. 7 is identical in form to Eqn. 2, with L/W as the appropriate aspect ratio for yaw as opposed to pitch motion.

$$C^*_{YM} \approx 0.09\left(1-\left(\frac{W}{L}\right)^2\right)\sin 2\psi - 0.04\left(\frac{W}{L}\right)\sin 4\psi \quad (7)$$

The overall yawing moments are reduced compared to the 2D case, although the aspect ratio dependent asymmetry represented by the 2nd term has increased.

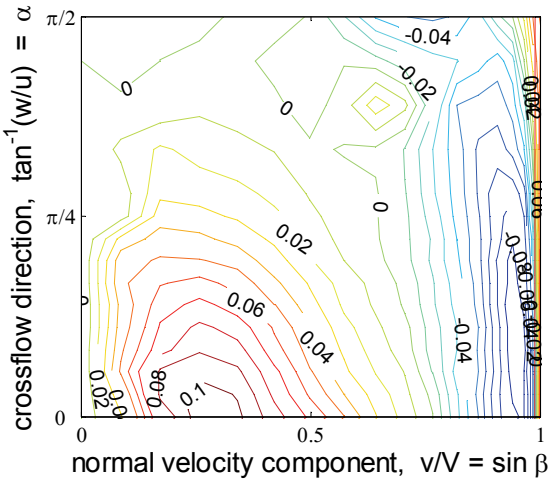

Fig.21 Variation of body axis yawing moment coefficient C^*_{YM} with normal velocity and crossflow direction for a cube [30]

Using the cube data from [30] as a starting point, Figure 21 shows the variation of body-axis yawing moment with the side face normal velocity component v/V and cross-flow direction $tan^{-1}(w/u)$. The two large 'separated flow' peaks at low and high incidence are clearly evident, the left hand peak from the left/right pair of faces, and the right hand peak from the front/rear side pair of faces. A similar picture is obtained if the front face parameters u/V and $tan^{-1}(w/v)$ are used, but with the relative extents of the two peaks reversed.

Symmetry considerations constrain the moment to zero along the right, left and upper edges of the plot. The moment characteristics are symmetric about $tan^{-1}(w/u) = 0$, and antisymmetric about $v/V = 0$.

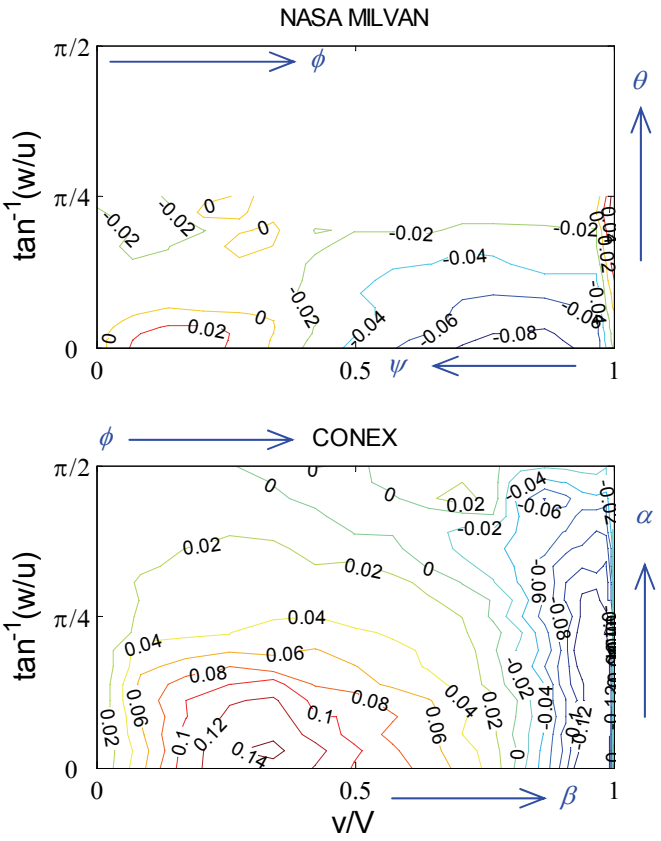

Fig.22 Variation of body axis yawing moment coefficient C^*_{YM} with normal velocity and crossflow direction for MILVAN and CONEX containers (data from [8][30])

Plotting yawing moment data for the CONEX [30] and MILVAN [8] containers (Figure 22) gives a very similar picture. For the CONEX container, essentially the same results are obtained for all three axes. For the MILVAN container the pitching moment data (plotted vs w/V and $tan^{-1}(v/u)$) is similar but less extensive, while the rolling moment data is unreliable (as noted in [8], possibly due to support interference effects from a large ventral strut mounting [28]).

4 3D Modelling

In order to illustrate the application of the modelling approach described above, the lateral aerodynamics (sideforce and yawing moment) of a CONEX container (Figure 23) will be briefly analysed, using data from Reference [30]. The aerodynamic characteristics of this container are similar in form to the more common MILVAN (Figures 11 and 20), but with rather larger separated flow increments, giving a more severe test. The baseline orientation for this container is with the longer side facing into the flow (ie L/W = 0.75, L/D = 1.0).

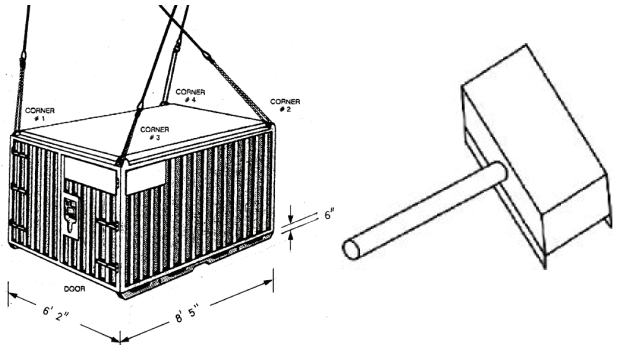

Fig.23 8ft×6ft×6ft CONEX container, with model as tested in [30]

4.1 Body-Axis Forces

Figure 24a shows the variation of the body-axis sideforce coefficient C_Y^* with the side face normal velocity component v/V and crossflow direction $\theta' = tan^{-1}(w/u)$. The reference area used is the side face area (6ft×6ft). The general behaviour is similar to that of the cube model shown in Figure 16, albeit with more pronounced separation bubble increments at low incidences, and a clear dip in base pressure at high incidence (Figure 18).

The first step in modelling this response is to remove the basic 'attached flow' linear response,

$$C^*_{Y,att} \approx +1.4 \sin\psi = -1.4\frac{v}{V} \qquad (8)$$

to give the 'separated flow' component ΔC_Y^*. (There is a small reduction from the general trend of Figure 18, probably due to a less intrusive strut geometry than in [28]).

Having done so, Figure 24b shows the separation bubble and base-dip sideforce increments much more clearly.

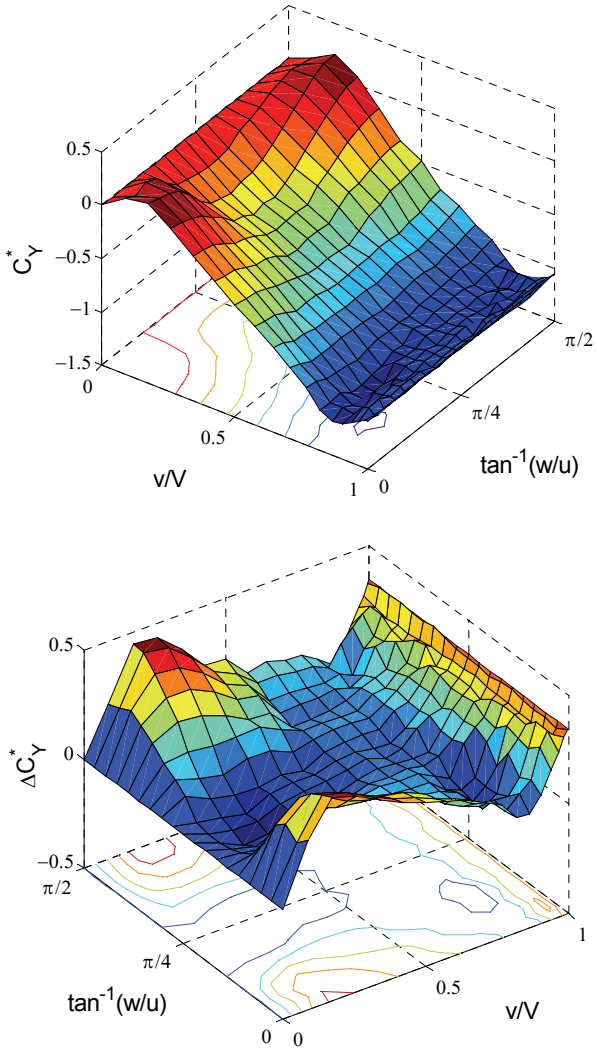

Fig.24 Effect of linear trend removal on CONEX body-axis side-force (data from [30])

Modelling these separated flow contributions can be done in two further steps.

Firstly, the increments at zero crossflow inclination (equivalent in this case to zero pitch angle) can be represented by two piecewise fits, Figure 25. The base-dip (blue line) rises linearly from zero at v/V ≈ 0.82 (55° yaw) to a maximum value of +0.35 with the flow perpendicular to the side face. The magnitude and onset of the base-dip is almost unaffected by crossflow direction. The separation bubble

increment (red line) has a peak of +0.45 at $v/V \approx 0.18$ (10° yaw), but reduces rapidly to zero at a crossflow inclination of 45°.

A more slender container (ie higher L/W) would have a smaller peak (Figures 11 and 18) at a lower incidence (lower α_R), but superimposed on the same 'attached flow' curve.

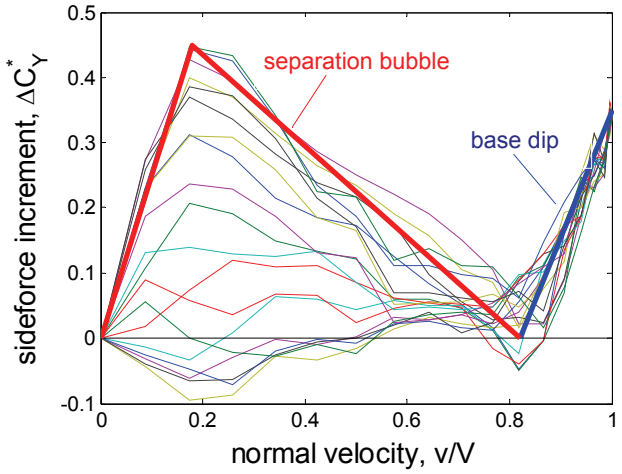

Fig.25 Piecewise linear fit to CONEX body-axis sideforce increment at zero pitch

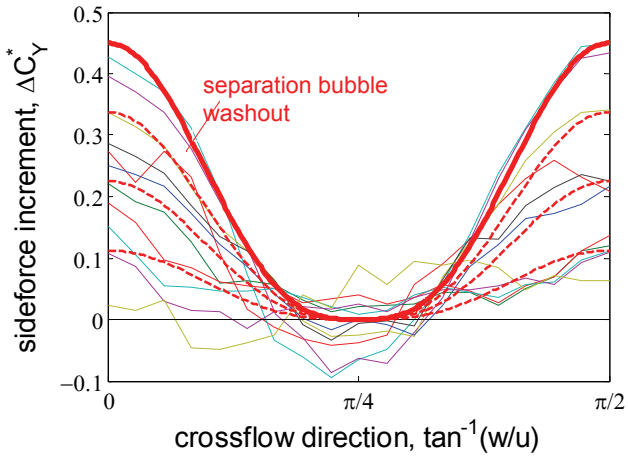

Fig.26 Separation bubble washout for CONEX body-axis sideforce increment

Secondly, having determined the separated flow increments at zero pitch/crossflow direction, it remains to model the variation with crossflow direction. The base-dip is essentially constant, but Figure 26 shows a strong crossflow effect on the low incidence bubble increment. A number of different functions could be used to model this effect – for the purposes of this discussion, a simple trigonometric washout was used

$$\Delta C_Y^* = \Delta C_{Y,0}^*(v/V) \times \left|\cos^3(2\theta')\right| \qquad (9)$$

where θ' is the crossflow (pitch) angle $tan^{-1}(w/u)$.

Taking Eqn (8), adding the piecewise linear separated flow fits of Figure 25, and then reducing the bubble contribution using Eqn. (9) gives the modelled sideforce characteristics shown in Figure 27.

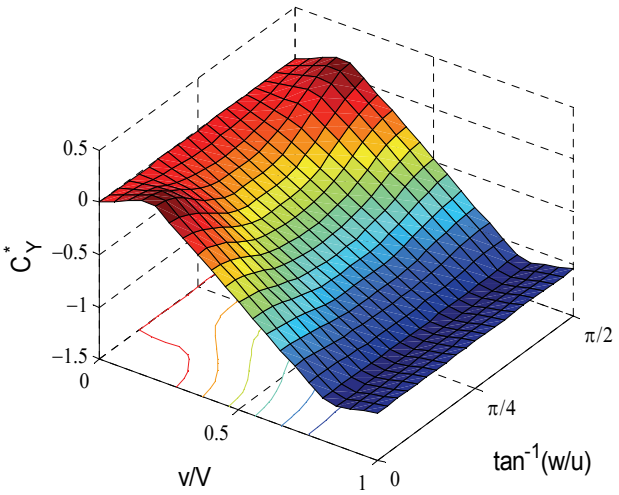

Fig.27 Basic 5-parameter fit to CONEX sideforce

The comparison with the experimental data of Figure 24a is very good, yet this surface is defined by just five parameters:

1) the basic attached flow slope (–1.4 to –1.5 for 3D containers),
2) the base pressure dip – governed by the aspect ratio,
3) the magnitude of the separation bubble – governed by the aspect ratio,
4) the peak incidence (α_R) – governed by the aspect ratio, and
5) the break between separation bubble and base-dip (0.8-09 for 3D containers),

of which only (3) and (4) show a significant variation with box geometry.

4.2 Body-Axis Moments

A similar modelling approach can be applied to body-axis moments, although the structure is

more complex because each moment has contributions from two pairs of faces.

Taking the CONEX yawing moment as an example, Figure 28 shows the effect of yaw angle on yawing moment coefficient at zero pitch (with moments non-dimensionalised using the side face area and length).

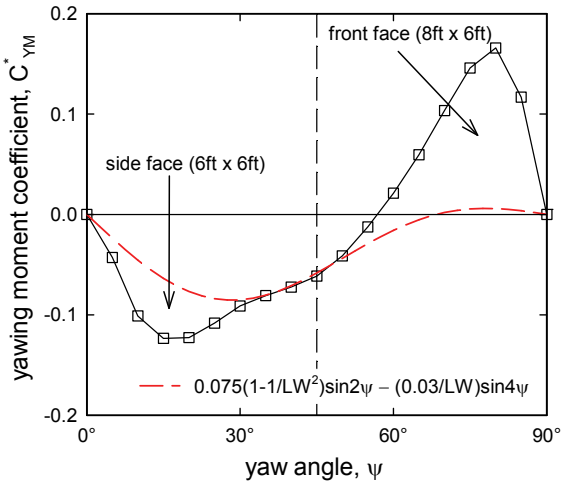

Fig.28 Attached & separated flow contributions to CONEX yawing moment (data from [30])

The basic attached flow moment (red dashed line) is modelled using the general form of Eqn. (7), with coefficients adjusted to match this specific case more closely.

$$C^*_{YM} = 0.075\left(1-\left(\frac{W}{L}\right)^2\right)\sin 2\psi - 0.03\left(\frac{W}{L}\right)\sin 4\psi \quad (10)$$

This can then be split into contributions from the two pairs of faces.

$$\begin{aligned} C^*_{YM,side} &= +0.075\sin 2\psi \\ C^*_{YM,front} &= -0.075\left(\frac{W}{L}\right)^2\sin 2\psi \\ &\quad -0.03\left(\frac{W}{L}\right)\sin 4\psi \end{aligned} \quad (11)$$

However, unlike the normal force 'attached flow', these components cannot be independent of the crossflow direction, since the yawing moments must go to zero at three out of four edges to the [normal velocity, crossflow] domain.

The side (shorter) face contribution will be governed by the normal velocity component v/V ($\equiv -sin\psi$) and crossflow (pitch) direction $\theta' = tan^{-1}(w/u)$. The front (longer) face contribution will be governed by the normal velocity component u/V ($\equiv cos\psi$ at zero pitch) and crossflow (roll) direction $\phi' = tan^{-1}(w/v)$. The $sin2\psi$ and $sin4\psi$ terms in Eqn. 11 can readily be converted into functions of u/V and v/V as required using standard trigonometry formulae.

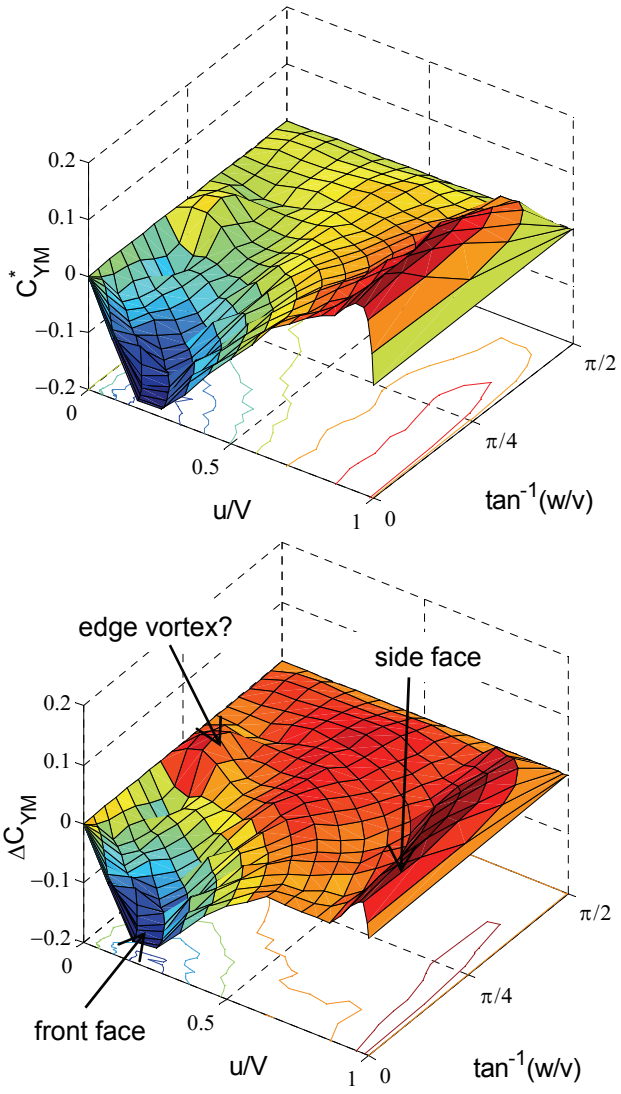

Fig.29 Effect of 'attached flow' removal on CONEX body-axis yawing moment

The variation with crossflow is rather less rapid than for the sideforce, and so a suitable washout function for a preliminary model is simply the cosine of the appropriate crossflow angle, so that

$$\begin{aligned} \Delta C^*_{YM,side} &= \Delta C^*_{YM,0}(v/V)\times\cos(\theta') \\ \Delta C^*_{YM,front} &= \Delta C^*_{YM,0}(u/V)\times\cos(\phi') \end{aligned} \qquad (12)$$

Given that the largest contribution to yawing moment for this particular container comes from the front and rear faces, Figure 29a plots the moment against the front face aerodynamic parameters u/V and $tan^{-1}(w/v)$. Subtracting the attached flow contribution of Eqn. 11 (washed out with crossflow angle using Eqn. 12) gives the nominal 'separated flow' component in Figure 29b.

This component is close to zero over most of the range, with two main peaks corresponding to the separation bubble contributions on the front/rear and side faces. The right-hand (and smaller) is due to the separation bubbles on the side (shorter) faces. The left-hand larger increment is due to the bubbles on the front/rear (longer) faces. There is an additional small peak half way along the left-hand edge, which may be due to the formation of a side-edge vortex. A similar small peak is seen in the MILVAN data of [8], when plotted in the same way.

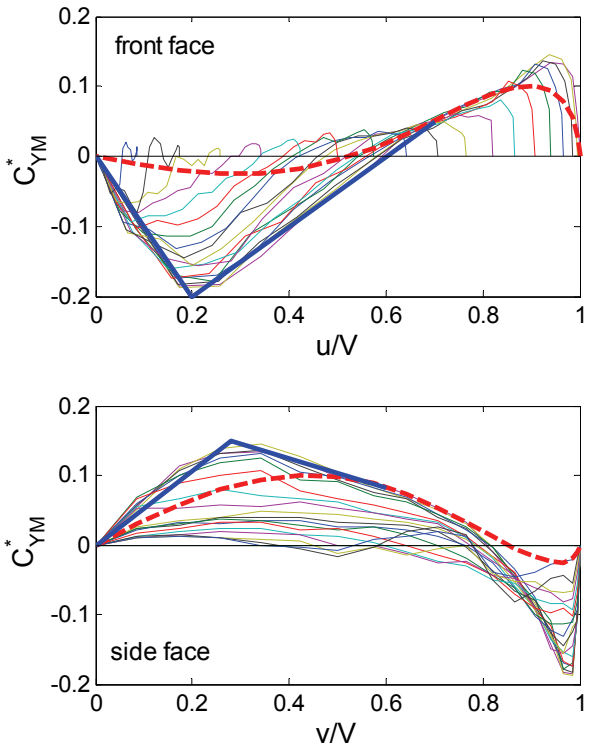

Fig.30 Piecewise linear fit to separated flow contributions to CONEX yawing moment

The two main separated flow contributions can be represented (as a first approximation) by piecewise linear fits, in a similar manner to the sideforce. Figure 30 shows the yawing moment plotted against both normal velocities (u/V and v/V), with Eqn. 11 shown by the red dashed line.

The front face bubble increment depends on u/V, with a peak of –0.18 at $u/V \approx 0.2$ (90–12° = 78° yaw), falling to zero at 0.7 (45° yaw). The side face bubble increment depends on v/V, with a peak of +0.07 at $v/V \approx 0.28$ (16° yaw), falling to zero at 0.6 (37° yaw). Within the constraints of a linear fit, these values are consistent with the bubble reattachment angles of Figure 7, and with complete flow reattachment at 45°.

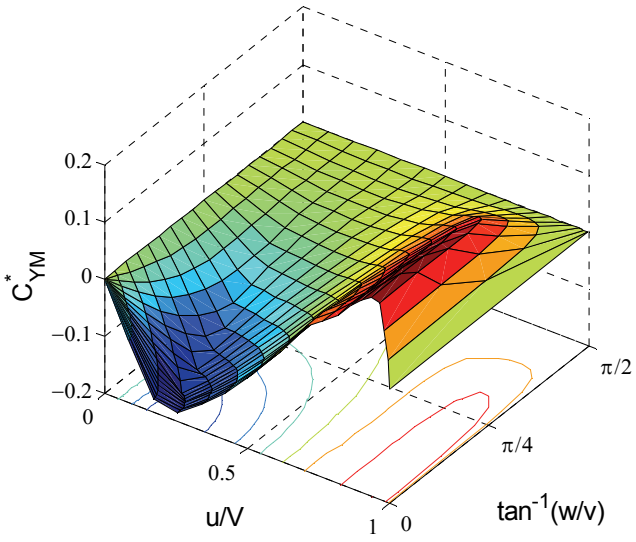

Fig.31 Basic 7-parameter fit to CONEX yawing moment

Finally, the two bubble contributions need to be washed out with the appropriate crossflow angle – using $cos^2(\theta')$ and $cos^2(\phi')$ as a first approximation gives the modelled yawing moment characteristics shown in Figure 31. Again, the comparison with the experimental data of Figure 29a is excellent, with only two more parameters needed to define the fit:

1) the basic symmetric attached flow slope (0.075 to 0.09 for 3D containers),
2) the asymmetric attached flow slope (0.03 to 0.04 for 3D containers),

3) the magnitude of the front face separation bubble – governed by the aspect ratio
4) the peak incidence (α_R) for the front face bubble – governed by the aspect ratio,
5) the magnitude of the side face separation bubble – governed by the aspect ratio
6) the peak incidence (α_R) for the side face bubble – governed by the aspect ratio, and
7) the upper extent of the separation bubble component (0.6 – 0.7 for 3D containers)

of which only (3) to (6) show a significant variation with box geometry.

Having split out the side face separation bubble contributions to force and moments, the effects of increased turbulence and Reynolds Number (early reattachment) and corner rounding (delayed bubble formation) can readily be included

5 Conclusions

A review of the aerodynamic characteristics of 2D and 3D rectangular boxes has shown that the basic forces and moments can be split into an 'attached flow' component and a 'separated flow' component. The first comprises the loads from the attached flow on the front face, the attached flow underlying the side face separation bubbles, and the fully separated base flow, and is independent of box geometry. The second component comprises the separated flow on the two side faces, which varies from full separation to a closed separation bubble depending on incidence and geometry.

Universal scaling rules have been determined. The 'attached flow' pressure distribution on a given face depends only on incidence, when the side face length L is used as a length scale. The 'separated flow' increment depends only on the underlying 'attached flow' pressure at the reattachment point. In turn, the bubble reattachment point depends only on incidence, when the adjacent front face length D is used as a length scale.

As a result, the aerodynamic characteristics of 2D and 3D boxes are found to be very similar, when non-dimensionalised correctly. Containers are rectangular bluff bodies, with the aerodynamic loads dominated by normal pressure forces. The loads therefore need to be considered in body axes, and not the universally used wind axes (which result in apparently highly complex variation in forces and moments with incidence). Further, the appropriate aerodynamic parameters are not the conventional angle of attack and sideslip angle, but the velocity components perpendicular to and parallel to each face.

The velocity component perpendicular to each face (u/V, v/V and w/V) governs the overall magnitude of the normal force and moments acting on that face, while the direction of the parallel (crossflow) velocity component governs which edge the flow separates from, and hence modifies the basic loading.

Recasting experimental data in this form, the aerodynamic characteristics of typical rectangular containers become much simpler in form, and more consistent in magnitude.

Body-axis forces are particularly straightforward. Each force component (axial, side, normal) is generated by the corresponding box face, with the basic attached flow component being directly proportional to the corresponding normal velocity component, so that for example $C_Y^* \propto v/V$. The 'lift-curve-slope' is essentially independent of aspect ratio, and ranges from −1.9 for 2D boxes to −1.5 for strut-mounted 3D box models to −1.2 for wire-mounted box models.

Superimposed on this basic force are small increments due to the separated flow. For normal velocities approaching 1 (ie flow perpendicular to the face), the wake flow structure appears to change, and the base pressure dips (becoming in general less negative). The magnitude of the base-dip depends on aspect ratio (reducing for more slender shapes, such as the MILVAN container), and appears to be significantly affected by support interference. At lower incidences the formation and disappearance of closed separation bubbles gives a more significant but also more localised increment, which depends on aspect ratio and on crossflow direction. For 0° and ±90° crossflow angle, the flow approaches an edge head-on and a closed separation bubble forms. For intermediate crossflow directions a closed bubble cannot

form and the increment disappears – but a small side-edge vortex may form instead.

Body-axis moments are a little more complex, because each moment component is generated by two pairs of faces. Nevertheless, the basic moment contributions remain simple and consistent when analysed in terms of normal and crossflow velocities. Each pair generates opposing moments that vary with the sine of twice the local incidence angle, with the overall moment depending on the relative sizes of the faces. The magnitude of this moment contribution is almost independent of aspect ratio, ranging from +0.12 for 2D prisms to +0.09 for 3D boxes (depending on support interference levels). An additional asymmetric moment appears to be generated by the forward facing side only. The moment contribution from each face slowly reduces to zero as the crossflow angle increases from 0° to ±90°.

Superimposed on the basic moment curve are two separate increments from the two pairs of separation bubbles. The magnitude of these depend on the corresponding normal velocity component, and again both reduce to zero as the crossflow angle increases from 0° to ±90° (rather more rapidly than for the attached flow components).

The universal nature of the 'attached flow' force and moment characteristics, coupled with 'separated flow' increments that can be adequately represented by piecewise-linear fits, means that modelling of the apparently complex aerodynamics of a container can be achieved with remarkably few parameters – of which only a small subset vary significantly with box geometry.

Further, this subset of parameters relates directly to the underlying flow physics. The magnitude and extent of the separated flow increments are directly governed by the magnitude and extent of the corresponding separation bubbles, which in turn depend on:

- incidence,
- box aspect ratio,
- corner radius,
- freestream turbulence level,
- Reynolds Number,
- wind tunnel support interference, and
- dynamic motion (pitch, yaw and roll rate)

The static modelling technique described here is therefore not just a modelling technique for flight dynamics simulations, but a prediction and analysis tool.

The universal scaling laws within the model structure (with a small number of empirical parameters derived from existing data) enable the *a priori* prediction of the aerodynamic characteristics of any new rectangular box load, and of the effects of geometry changes for an existing container. Extrapolation of existing data to incidence angles outside the original database becomes much more straightforward.

The relationship between bubble size and aerodynamic characteristics clarified by the model structure also provides a rational basis for correction/extrapolation of experimental data for turbulence, Re and tunnel interference effects.

Finally, the split into attached and separated load components gives a physical basis for the modelling of *dynamic* aerodynamic characteristics – for example the complex effects of motion frequency on the yaw damping derivative, for a MILVAN model reported in [10]. A split into quasi-steady 'attached flow' and time-lagged 'separated flow' components has been very successful in the modelling of high-incidence aerodynamics of combat aircraft [34], and recent work at City suggests that similar success may be obtained for container dynamics.

Nomenclature

C_X^*	body-axis axial force component, based on front face area
C_Y^*	body-axis sideforce component, based on side face area
C_Z^*	body-axis normal force component, based on top face area
C_{RM}^*	body-axis rolling moment component, based on side face area and length
C_{PM}^*	body-axis pitching moment component, based on top face area and length
C_{YM}^*	body-axis yawing moment component, based on side face area and length
C_D, C_d	wind-axis drag, based on projected frontal area
C_L, C_l	wind-axis lift, based on projected frontal area
C_m	wind-axis pitching, based on projected frontal area and depth
C_{pB}	base pressure
C_{pmax}	maximum bubble suction pressure
D	box depth (or height)
D_f	projected depth, $= D\cos\alpha + L\sin\alpha$,
L	streamwise box length ($= H$)
q, Q	dynamic pressure, $= \frac{1}{2}\rho V^2$
S	separation bubble length
u,v,w	Cartesian velocity components
V	freestream velocity
W	box width
x,y,z	Cartesian coordinates
α	angle of attack, $= \tan^{-1}(w/u)$
α_R	bubble reattachment incidence
β	sideslip angle, $= \sin^{-1}(v/V)$
θ, ψ	Euler pitch and yaw angles
ϕ'	front face crossflow, $= \tan^{-1}(w/v)$
θ'	side face crossflow, $= \tan^{-1}(w/u)$
ψ'	top face crossflow, $= \tan^{-1}(v/u)$

References

[1] Matheson, N., "The Stability of Portable Bridges Carried on Slings Beneath Helicopters", Aerodynamics Report 154, DSTO, January 1980

[2] Sheldon, D.F. and Pryor, J., "Study in Depth of a Single Point and Two Point Lateral and Tandem Suspension of Rectangular Box Loads", Technical Note AM/38, Royal Military College of Science, 1973

[3] Stuckey, R.A., "Mathematical Modelling of Helicopter Slung-Load Systems", DSTO–TR–1257, December 2001

[4] Cicolani, L.S. and Ehlers, G.E., "Modelling and Simulation of a Helicopter Slung Load Stabilization Device", *American Helicopter Society 58th Annual Forum*, Montreal, Canada, June 2002

[5] Pavel, M.D., "Mathematical Modelling of Tandem Helicopters with External Sling Loads for Piloted Simulations", AIAA-2006-6617, *AIAA Modelling & Simulation Technologies Conference*, Hilton Head, August 2007

[6] Kendrick, S. and Walker, D.J., "The Modelling, Simulation and Control of Helicopters Operating With External Loads", *62nd American Helicopter Society Annual Forum*, Phoenix, May 2006

[7] Duque, E. P.N. *et al*, "Reynolds-Averaged Navier-Stokes Simulations of Helicopter Slung Loads", *AHS International 4th Decennial Specialists' Conference on Aeromechanics*, San Francisco, January 2004

[8] Cicolani, L. and Kanning, G., "A Comprehensive Estimate of the Static Aerodynamic Forces and Moments of the 8- by 8- by 20-Foot Cargo Container", NASA TM 89433, May 1987

[9] ESDU, "Fluid Forces, Pressures and Moments on Rectangular Blocks", ESDU datasheet 71016, November 1978

[10] Simpson, A. and Flower, J.W., "Unsteady Aerodynamics of Oscillating Containers and Application to the Problem of Dynamic Stability of Helicopter Underslung Loads", paper 13 in AGARD CP-235 *Dynamic Stability Parameters*, November 1978

[11] Poli, C. and Cromack, D., "Dynamics of Slung Bodies Using a Single-Point Suspension System", *Journal of Aircraft*, Vol 10 No 2, February 1973, pp80-86

[12] Shaughnessy, J.D., Deaux, T.N. and Yenni, K.R., "Development and Validation of a Piloted Simulation of a Helicopter and External Slung Load", NASA TP-1285, January 1979

[13] Weber, J. M., Liu, T. Y. and Chung, W., "A Mathematical Simulation Model of the CH-47B Helicopter", NASA TM-84351, August 1984

[14] Feaster, L., Poli, C. and Kirchoff, R., "Dynamics of a Slung Load", *Journal of Aircraft*, Vol. 14, No. 2, February 1977, pp115-121

[15] Ronen, T., "Dynamics of a Helicopter with a Sling Load", Ph.D. Thesis, Dept. of Aeronautics and Astronautics, Stanford University, August 1985 (also AIAA-86-2288)

[16] Cicolani, L.S., da Silva, J.G.A., Duque, E.P.N. and Tischler, M.B., "Unsteady Aerodynamic Model of a Cargo Container for Slung-Load Simulation," *The Aeronautical Journal*, July 2004

[17] Norberg, C., "Flow Around Rectangular Cylinders: Pressure Forces and Wake Frequencies", *Journal of Wind Engineering and Industrial Aerodynamics*, Vol 49, 1993, pp187-196

[18] Matsumoto, M. et al, "Aerodynamic Effects of the Angle of Attack on a Rectangular Prism", *Journal of Wind Engineering and Industrial Aerodynamics*, Vol 77&78, 1998, pp531-542

[19] Laneville, A. and Lu, Z.Y., "Mean Flow Patterns Around Two-Dimensional Rectangular Cylinders and Their Interpretation", *Journal of Wind Engineering and Industrial Aerodynamics*, Vol 14, 1983, pp387-398

[20] Laneville, A., Gartshore, I. S. and Parkinson, G. V., "An Explanation of Some Effects of Turbulence on Bluff Bodies', 4th International Conference on Wind Effects on Buildings and Structures, London, September 1975

[21] Robertson, J.M. et al, "Wall Pressures Of Separation-Reattachment Flow on a Square Prism in Uniform Flow", *Journal of Industrial Aerodynamics*, Vol 5, 1979, pp179-186

[22] Sant'Anna, F.A.D-M., Laneville, A., Trepanier, J.Y. and Lu, Z.Y., "Detailed Pressure Field Measurements for Some 2-D Rectangular Cylinders", *Journal of Wind Engineering and Industrial Aerodynamics*, Vol 28, 1988, pp241-250

[23] Mulhearn, P.J., "Stagnation and Reattachment Lines on Cylinder of Square Cross-Section in Smooth and Turbulent Flows", *Nature (Physical Science)*, Vol 241, 26th February 1973, pp165-167

[24] Leishman, J.G., *Principles of Helicopter Aerodynamics*, 2nd edition, Cambridge University Press, 2006

[25] Windsor, R. I., "Wind Tunnel Tests of Two Models of Rectangular Containers", Wind Tunnel Report No 573. University of Maryland, Glenn L Martin Wind Tunnel, College Park, Maryland, January 1970

[26] Briczinski, S.J. and Karas, G.R., "Criteria for Externally Suspended Helicopter Loads", USAAMRDL TR-71-61, November 1971

[27] Watkins, T.C., Sinacori, J.B. and Kesler, D.F., "Stabilization of Externally Slung Helicopter Loads", USAAMRDL TR-74-42, August 1974

[28] Laub, G.H. and Kodani, H.M., "Wind Tunnel Investigation of Aerodynamic Characteristics of Scale Models of Three Rectangular Shaped Cargo Containers", NASA TM-X 62169, July 1972

[29] Cicolani, L.S., da Silva, J.G.A., Duque, E.P.N. and Tischler, M.B., "Unsteady Aerodynamic Model of a Cargo Container for Slung-Load Simulation," *The Aeronautical Journal*, July 2004

[30] Rosen, A., Cecuttam S. and Yaffe, R., "Wind Tunnel Tests of Cube and CONEX Models", Technion report TAE-844, November 1999

[31] Sheldon, D.F. and Pryor, J., "Study in Depth of a Single Point and Two Point Lateral and Tandem Suspension of Rectangular Box Loads", Technical Note AM/38, Royal Military College of Science, May 1973

[32] Sheldon, D.F. and Pryor, J., "A Study on the Stability and Aerodynamic Characteristics of Particular Military Loads Underslung from a Helicopter", Technical Note AM/40, Royal Military College of Science, April 1973

[33] Sheldon, D.F. and Pryor, J., "The Aerodynamic Characteristics of Various Rectangular Box and Closed Cylinder Loads", Technical Note AM/41, Royal Military College of Science, April 1973

[34] Greenwell, D.I., "A Review of Unsteady Aerodynamic Modelling for Flight Dynamics of Manoeuvrable Aircraft", AIAA-04-5276, *AIAA Atmospheric Flight Mechanics Conference*, August 2004

Appendix A

A general fit to the underlying attached flow pressure distribution for the front face of a 2D rectangular prism, for pitch angles from 0° to 90° is

$$C_p = p\left(1 - C_{pB}\right) + C_{pB} \qquad \text{(A1a)}$$

where the basic pressure distribution shape is given by

$$p = \left(1 - w^2\right)^{1/4} \qquad \text{(A1b)}$$

and the asymmetry by

$$w = 2\left(\frac{x}{L}\right)^{1/n} - 1 \qquad \text{(A1c)}$$

where n is an empirically determined function of incidence.

Figure A1 shows that this single equation can cover both front and side face flows, despite the apparently very different form they take.

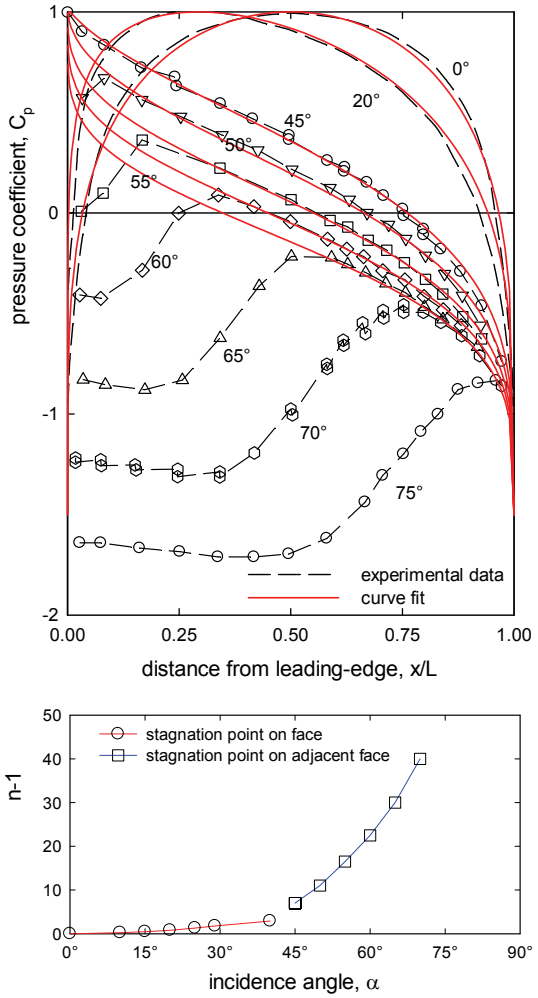

Fig.A1 Fit to 'attached' flow component on 'front' face (data from [21])

Copyright Statement